Tuning the electro-optical properties of nanowire networks

Koorosh Esteki,[1] Hugh G. Manning,[2,3] Emmet Sheerin,[2,3] Mauro
S. Ferreira,[2,4] John J. Boland,[2,3] and Claudia Gomes da Rocha[1,5]

[1]*Department of Physics and Astronomy,*
University of Calgary, 2500 University Drive NW,
Calgary, Alberta T2N 1N4, Canada.
[2]*Advanced Materials and Bioengineering Research (AMBER) Centre,*
Trinity College Dublin, Dublin 2, Ireland.
[3]*School of Chemistry, Trinity College Dublin, Dublin 2, Ireland.*
[4]*School of Physics, Trinity College Dublin, Dublin 2, Ireland.*
[5]*Hotchkiss Brain Institute, University of Calgary,*
3330 Hospital Drive NW, Calgary, Alberta T2N 4N1, Canada.

Abstract

Conductive and transparent metallic nanowire networks are regarded as promising alternatives to Indium–Tin–Oxides (ITOs) in emerging flexible next-generation technologies due to their prominent optoelectronic properties and low-cost fabrication. The performance of such systems closely relies on many geometrical, physical, and intrinsic properties of the nanowire materials as well as the device-layout. A comprehensive computational study is essential to model and quantify the device's optical and electrical responses prior to fabrication. Here, we present a computational toolkit that exploits the electro-optical specifications of distinct device-layouts, namely standard random nanowire network and transparent mesh pattern structures. The target materials for transparent conducting electrodes of this study are aluminium, gold, copper, and silver nanowires. We have examined a variety of tunable parameters including network area fraction, length to diameter aspect ratio, and nanowires angular orientations under different device designs. Moreover, the optical extinction efficiency factors of each material are estimated by two approaches: Mie light scattering theory and finite element method (FEM) algorithm implemented in COMSOL Multiphysics software. We studied various nanowire network structures and calculated their respective figures of merit (optical transmittance versus sheet resistance) from which insights on the design of next-generation transparent conductor devices can be inferred.

I. INTRODUCTION

Transparent conducting films are necessary components for various modern electronic and optoelectronic devices[1, 2]. Particularly, transparent conductors (TCs) made of metallic nanowire networks (NWNs)[3] are a promising alternative for the most commonly used Indium-Tin-Oxides (ITOs)[4] which has been dominating the planar display technology in the last years. Nonetheless, the high cost and limited supply of indium combined with ITO's brittle nature and expensive fabrication process (via vapor phase sputtering[5]) have prompted scientists to search for replacement materials[6, 7]. Metallic NWNs have demonstrated mechanical deformability, a low cost of fabrication along with high optical transmission, and high electrical/thermal conductivity[8–10]. Other technologies in which NWNs have demonstrated noteworthy operation efficiency include solar cells[11], flexible displays and touch screens[12], thin-film heaters[13], wearable sensors[14], neural interfaces[15], and neuromorphic computing[16, 17], just to name a few. As discussed by Bae et al [18], TCs need to exhibit high optical transmittance, typically $\sim 90\%$, while the electrical sheet resistance (R_s) depends upon the device's operation and function. From touch screens, flexible displays, up to solar cells, these devices typically operate with distinct resistance values ranging from $\sim 500\,\Omega/\square$ to lower as $\sim 1\,\Omega/\square$ [18]. For this reason, it is important to fine-tune these two quantities (transmittance and resistance) when designing TC devices for a given function. For this purpose, a variety of materials including conductive polymers[19], graphene[20], carbon nanotubes[21], ultra-thin metal films[22], and metallic nanowires [1, 23–25] have been tested as TCs to discover the optimum trade-off between electrical conduction and optical transmittance[26]. Therefore, a figure of merit (FOM) analysis is commonly employed in which optical transmittance (T) versus sheet resistance (R_s) for distinct raw materials, device designs, and intrinsic physical properties[27, 28] are obtained to measure the performance of the material as a transparent conductive medium.

Recently, many computational and experimental studies have been devoted to understanding FOM trends to determine the optimal design of metallic NWNs[29–36] as TCs. The electro-optical properties of these networks depend on a variety of control parameters including structural ones such as nanowire aspect ratio[31, 37, 38] (AR) defined as the nanowire length (L) divided by the nanowire diameter (D), network density (n) defined as the number of nanowires per unit of area, nanowires' orientation[39], nanowire's curva-

2

ture effects or wire persistent lengths[40–44], and network area fraction (AF). Moreover, electro-optical parameters include junction resistances between nanowires[36] (R_{jxn}), inner nanowire resistances defined as $R_{in} = \rho L/A$ with A being the cylinder cross-sectional area and ρ the resistivity, and optical extinction coefficients[29, 30]. Finally, geometrical parameters related to device-design such as electrode shapes[45] and the addition of transparent grid patterns[46, 47], all together, affect the overall percolative nature of conduction in the system and its light transmission. For instance, it has been demonstrated that the R_s and AF has a nonlinear and inverse relationship; as the AF ratio increases R_s will be reduced meaning that the increase in area coverage improves electrical transmission by the creation of additional parallel paths across the device[31]. If the wire density is enhanced at a fixed nanowire AR, the R_s will be reduced nonlinearly, with the resistance of a dense NWN transitioning from a percolative to bulk-like behavior regime, saturating at a steady resistance value that depends on the bulk material properties and dimensions of the film[33, 48]. At the same time, this increase in density reduces optical transparency as a result of the increase in the area coverage as more nanowires are added per unit of area. But as mentioned above, it is not only wire density that can affect the electro-optical characteristics of NWNs[49]. Such multi-dimensional parameter phase-space has led researchers to engineer optimum parameter combinations and settings to deliver the best FOM trade-off of highest possible transparency and adjustable sheet resistance range suitable for a given TC technology[28, 36].

In addition to resistance and transmittance, electromagnetic emissions generated by device components at high frequencies, e.g. radio frequency (RF), can not only cause malfunctions and shorten the operational lifetime of the device but can also affect human health[50, 51]. Hence, during the fabrication of TC films, high electromagnetic interference shielding effectiveness (EMI SE) needs to be taken into consideration[46, 52, 53]. For instance, ITO films are reported to exhibit $R_s \sim 10\,\Omega/\square$ and optical transmittance of $T \sim 90\%$ while silver (Ag) NWNs reveal $R_s \sim 20\,\Omega/\square$ and optical transmittance of $T \sim 91\%$[54]. Additionally, ITO is known to exhibit EMI SE of 14 decibels (dB) @ 84.1% transmittance within $0.5 - 3.0$ GHz frequency range, whereas Ag NWNs exhibit EMI SE of 13.5 dB @ 90.3% transmittance within the same frequency range[55].

In this manuscript, we have conducted an in-depth computational study of randomly oriented and grid-patterned NWNs and compared their FOM (optical transmittance versus sheet resistance) for a variety of metallic nanowire materials, namely silver (Ag), aluminum

(Al), and gold (Au). Copper (Cu) NWNs will also be briefly discussed in this work as a follow up from our previous publication in reference[30]. In addition, the impact of the nanowires' alignment on the network electrical conductivity is studied. The optical transmittance calculations are carried out using the Mie light scattering theory (MLST)[56] and FEM employing COMSOL$^{\circledR}$ Multiphysics software[57], and the sheet resistance is determined using modified nodal analysis (MNA) for a resistive circuit network[58–60]. We have found that an optimum trade-off between optical transmittance and sheet resistance can be tuned by playing with the grid-pattern design of the networks, density, nanowire orientation, and material properties. Other relevant network parameters we have considered in our simulations include nanowire aspect ratio (AR), and coverage area fraction (AF). Furthermore, we have studied hybrid network structures composed of straight and curved nanowires modeled as a semi-circle nanoring and examined the effect caused by curvature on the overall conductance response of the film. The outcomes of this research will contribute to the design of cutting-edge TC devices made of metallic NWNs with optimal electro-optical performance by suggesting materials and device layouts that can be tailored for each type of device.

II. METHODS

To capture the combined electrical and optical properties of distinct NWN systems, we have developed a computational method that carries out electrical resistance and optical transmission calculations independently. The first stage of the simulation consists of generating a random NWN which is done via Monte-Carlo procedure. Line segments representing cylindrical nanowires are randomly distributed within a squared area of dimensions $W \times W$. Overlapping line segments characterize inter-nanowire connections and all intersections are detected to determine the network connectivity prior to the electrical transport simulations. The whole network system is mapped as a resistive circuit network containing multiple voltage nodal points and inner/junction resistances. To calculate the network sheet resistance, a two-terminal set up with a current source attached to the network is considered in which Ohm's law combined with Kirchhoff circuit laws is applied as described in detail in previous works[29, 30, 59]. The optical property calculations are performed by employing two techniques, Mie light scattering theory (MLST)[56] and FEM approach using the COMSOL$^{\circledR}$

4

Multiphysics software[57]. In the MLST formalism, optical properties are obtained by the exact analytical solutions to Maxwell's equations accounting for the scattering of electromagnetic radiation by particles[56]. One of the limitations of the MLST method is that its exact solution is restricted to only highly symmetrical geometries such as cylinders, spheres and spheroids[61] in which one can write separate radial and angular dependence of solutions according to the object's coordinate systems. The description of the exact electromagnetic wave solution for MLST is detailed in the book by Bohren and Huffman[56]. Other relevant references for the theory are [62, 63]. Here, we considered the proposed Mie electromagnetic wave scattering solution for a uniform infinite cylinder implemented in MATSCAT software[64] developed by Schäfer[65, 66] to compute the extinction efficiency coefficients given by $Q_{ext} = Q_{sca} + Q_{abs}$ where Q_{ext}, Q_{sca}, and Q_{abs} are the extinction, scattering, and absorption coefficients, respectively.

An alternative tool for computing the optical transmission of particles with irregular shapes, such as curved nanowires, is COMSOL® Multiphysics[57] interface modeling. We utilized COMSOL to model the scattered electric field of the object at nano and microscales to solve Maxwell's differential equations in two- and three-dimensional space domains. The FEM analysis was carried out by the "electromagnetic waves" and the "frequency domain" (EMW) interfaces available in the "radio frequency" (RF) module. The details on the mathematical formulation of FEM algorithms lie outside the scope of the present study, yet we provide additional tests and results in our supplemental information (SI)[67]. The optical efficiencies calculated by MATSCAT[64] are set as our benchmark method from which we could reproduce experimental FOM trends as shown in our previous works[29, 30]. In this way, settings for COMSOL modeling were done having MATSCAT results as a reference for uniform and infinite structures. For instance, we have constructed an infinite cylinder model in COMSOL by building a two-dimensional circular disk representing the cross-section of a cylindrical nanowire surrounded by an outer circular disk which is the perfectly matched layer (PML) to shorten the physical domain in an infinite space medium. The simulation domain was adequately discretized into a physics-controlled meshing and the material of the inner disk was set to match the known properties of the nanowire of interest, integrated with air as the surrounding medium. The overall effective optical response is evaluated by the impact of a background electromagnetic wave ($E_0 = 1$ V/m) on the surface of the nanowire where the wavelength of the plane wave was swept in the range of $\sim 300 - 1200$ nm

5

(for the case of the three-dimensional curved and straight nanowire is $\sim 350 - 750$ nm, cf. Figure S4 in the supplemental information[67]). We have used the incorporated wavelength-dependent permittivity information in COMSOL's material database, taken from Johnson and Christy[68]. Suitable boundary conditions such as perfect electric conductors (PECs) and scattering boundary conditions along with the surface and volume integrations were required to compute the absorption, scattering, and extinction coefficients as detailed in the supplemental information. The target orientation was set in such a way that the principal axis of an infinite cylinder is normal to the propagation of the electromagnetic field. Like MATSCAT, we have calculated and averaged both orthogonal polarizations of the incident light, one with an electric field perpendicular to the cylinder axis and another parallel to it.

Q_{ext} significantly depends on several factors including the incident beam wavelength, the diameter of the nanowire, and the complex refractive index of the nanowire material. Here, we obtained the maximum light transmission which is the measure of the extinction efficiency coefficient at normal light incidence to the TC film. The obtained extinction efficiency coefficients are used as input information for the Beer-Lambert law[69, 70] to compute the optical transmittance (T) as:

$$T = \exp\left\{-AF \times Q_{ext}\right\} \tag{1}$$

with AF being the coverage area fraction of the NWN. The AF can be estimated without considering the excluded area of overlapping nanowires with $AF = n \times L \times D$, n being the total number of wires per unit of area. Such effective AF, however, comes as a first-order approximation since it overestimates the coverage area of the NWN by over-counting the contact area between two nanowires. To tackle this problem, our simulations were built to compute the exact AF of a virtual NWN deposited over a square device area using image processing functions that distinguish nanowire objects from the image background. From a top-view perspective, a single nanowire covers an area of $L \times D$ but when two wires connect, for instance, our implementation calculates the exact area covered by the two overlapping wires by computing their pixel information.

To estimate the EMI SE of the NWNs, we consider the contribution from the sum of three EMI losses which are microwave absorption (SE_A), microwave reflection (SE_R), and multiple reflections (SE_{MR})[71]. The latter is considered as a correction factor whose value

6

may be zero, positive or negative. According to the mathematical formalism of SE_{MR} that is only dependent upon SE_A for $SE_A > 10$, SE_{MR} can be neglected[72, 73]. An independent frequency relationship (larger than 30 MHz)[74] between EMI SE and R_s can be derived when $\sigma/(\omega\epsilon_0 \gg 0)$[71, 75] where σ is the material conductivity, ω is the angular frequency, and ϵ_0 is the permittivity of vacuum. This relation is given by the following expression[71–76]:

$$\text{EMI SE} = 20 \log_{10}\left(1 + \frac{Z_0}{2R_s}\right) \tag{2}$$

where $Z_0 = 376.7\,\Omega$ is the wave impedance of free space. This equation illustrates how the sheet resistance affects the EMI SE performance, indicating the importance of quantifying the electrical properties of TC films to meet specific technological applications.

III. RESULTS AND DISCUSSION

Here, we present the FOMs (optical transmittance versus sheet resistance) obtained numerically for several NWN devices and materials, including Al, Ag, and Au. To tune the electrical and optical responses of NWNs, we manipulated the onset of percolation and the intrinsic features of the nanowires. Figure 1 depicts schematic images of NWN systems addressed in this work: (a) regular random NWNs, (b) random NWNs with a transparent grid-patterned over it, (c) NWNs made of oriented nanowires by fixing their maximum angle with the horizontal axis at a certain value θ_{max}, and (d) NWNs made of oriented nanowires with the transparent grid pattern. The effects caused by the presence of curved nanowires in the NWNs will also be investigated. Experimental micrograph images of NWNs evidence the presence of curved or even L-shape wires in the networks, therefore hybrid NWNs are introduced to illustrate more realistic physical systems.

The NWNs have dimensions of $30 \times 30\,\mu m$ which means that the source and drain electrodes are placed $30\,\mu m$ apart. The aspect ratios ($AR = L/D$) of the nanowires investigated in this work are distributed between 100 to 228. We ran simulations to determine FOM for all system cases depicted in Figure 1 for different nanowire materials including Al, Ag, and Au. The angular constraint of the nanowires with respect to the horizontal x-axis was set in the range of $\pm 36^o$ up to $\pm 75^o$. We performed our simulations by tuning all the physical parameters including nanowire length and diameter, NWN density, and area fraction. The average sheet resistance and its standard deviation were obtained for an ensemble of
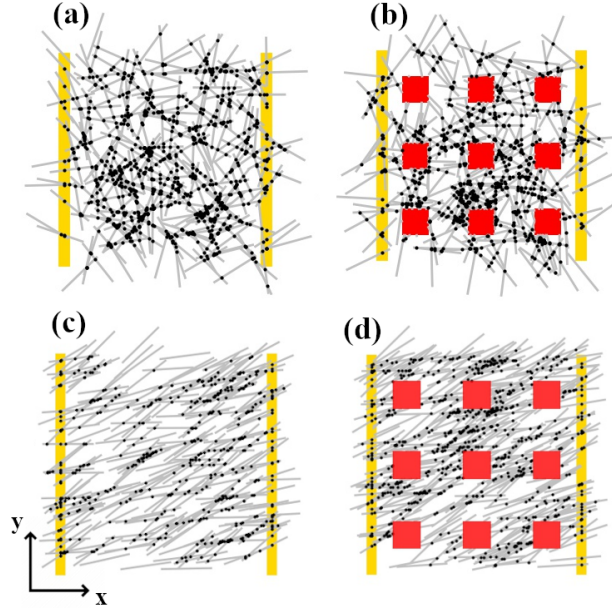
FIG. 1: (color online) Schematics of four NWN systems studied in this work. In all panels, grey lines represent nanowires and black circles mark their contact points. Golden vertical lines represent metallic electrodes in which a current source (not shown) is attached. The device size is $30 \times 30 \, \mu m$ and all nanowires have a fixed length of $L = 7 \, \mu m$. (a) A standard random NWN is presented with wire density of $n = 0.3$ nanowires/μm^2. (b) A 3×3 transparent grid (red squares) is patterned over a random NWN with wire density of $n = 0.3$ nanowires/μm^2. This strategy targets improving the transparency of the films. Each square is $4 \times 4 \, \mu m$ in size. (c) A random NWN of wire density of $n = 0.4$ nanowires/μm^2 with angular constraint. Each nanowire is placed randomly over the device area, however, their orientation is capped by a maximum angle (θ_{max}) measured with respect to the horizontal axis. In this example, $\theta_{max} = \pm 45^o$. (d) NWN with the same structural characteristics as in panel (c) but with the transparent grid (red squares).

NWNs of fixed density containing 10 random spatial configuration samples. We assigned the corresponding resistivity values of $\rho = 19.26 \, n\Omega m$, $\rho = 16.85 \, n\Omega m$, and $\rho = 25 \, n\Omega m$ for Ag[29, 36], Al[77], and Au[78, 79], respectively. Junction resistances can fluctuate considerably as reported in previous works[30, 36, 77–80] and, for the sake of simplicity, we fixed this quantity at $R_{jxn} = 50 \, \Omega$ for the results shown in this work. This is just a gauge junction resistance value that we kept fixed to reduce our parameter phase space. Any correction to the sheet resistance due to alterations in R_{jxn} can be obtained by extrapolation methods as we conducted in a previous work[59].

The optical extinction efficiency coefficients were calculated using both MLST[64] and FEM methods from which Q_{ext} was determined for the visible light wavelength range of $400 - 700$ nm. Optical extinction efficiency coefficients (Q_{ext}) for metallic nanowires made of four different materials (Ag, Al, Au, and Cu) and diameters of $D = 30$ nm and $D = 50$
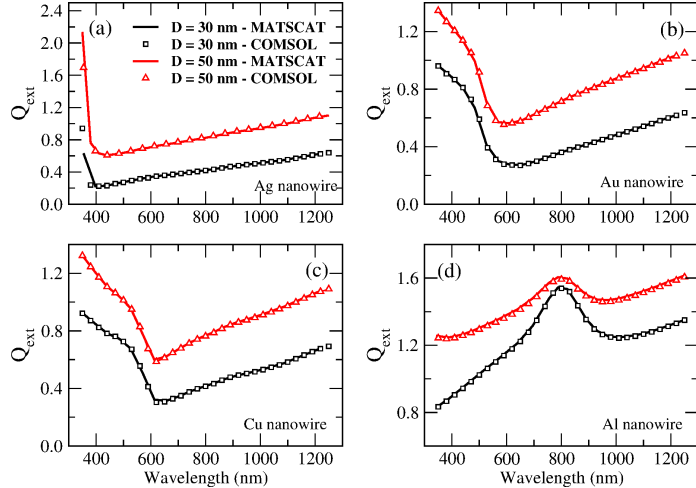
FIG. 2: (color online) Calculated optical extinction efficiency coefficients (Q_{ext}) of an individual nanowire as a function of light wavelength ranging $300 - 1200$ nm. All Q_{ext} values were computed based on averaging the two perpendicular electric field polarizations. Each panel presents the results for a metal: (a) Ag, (b) Au, (c) Cu, and (d) Al. Legend depicted on panel (a) applies to all other panels. All panels contain results for nanowires of two diameters: $D = 30$ nm (black symbols and lines) and $D = 50$ nm (red symbols and lines). The simulations were carried on with MATSCAT[64] (full lines) and COMSOL® Multiphysics software[57] (symbols).

nm were calculated as a function of the light wavelength (λ) ranging $300 - 1200$ nm (cf. Figure 2). The determination of FOM for NWN TCs depends on this coefficient combined with the numerically computed AF of the NWNs that gives the optical transmission as in equation (1). To quantify the optical transmission of all systems studied in this work, we used the Q_{ext} value at $\lambda = 546$ nm. Q_{ext} was determined for an infinite cylinder using two distinct light scattering methods, MATSCAT[64] and EMW available in the RF module of COMSOL® Multiphysics software[57]. Figure 2(a-d) demonstrates that the two methods agree within the whole range of wavelengths and cylinder diameters. Local electric field enhancement is material sensitive with Al nanowire demonstrating the strongest electric field scattering distributions at larger wavelengths.

It is challenging to accurately produce FOMs for a variety of materials and study all the influences caused by either the nature of the materials or the structural aspects of the TC NWN devices because high transparencies demand decreasing area fraction whereas low sheet resistances require the inverse. It is a trade-off analysis that can be investigated through computational simulations such as those conducted in this work. Figure 3 presents averaged $R_s \times T$ over an AR range of $100 - 228$ for various NWN densities and, consequently, various AFs. Figures 3(a,b) show the calculated FOMs for standard and transparent grid-

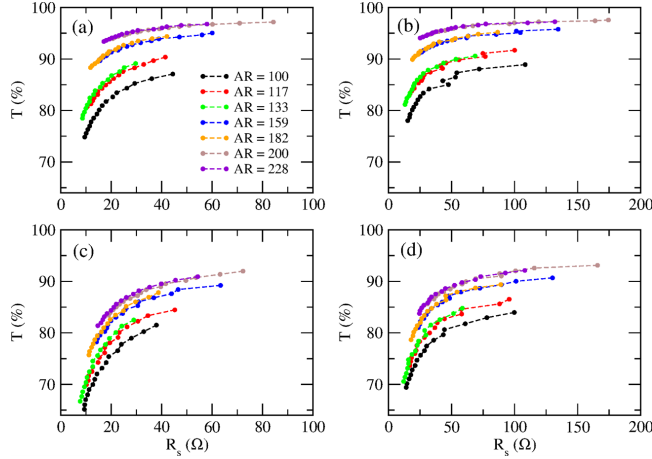FIG. 3: (color online) Average optical transmittance in percentage (T) versus average sheet resistance (R_s) results for different nanowire aspect ratios (AR). Every data point is averaged over 10 random NWN samples of a given density n. All systems are $30 \times 30\,\mu m$ in size. NWN densities were varied from 0.3 up to 0.7 nanowires/μm^2 in steps of 0.025. Top panels (a,b) show results for NWN TC devices made with Ag nanowires whereas bottom panels (c,d) are for Al nanowires. Left panels (a,c) exhibit the FOM for standard random NWNs whereas right panels (b,d) are for transparent grid-pattern NWNs. The latter was built with a 3×3 transparent grid as depicted in Figure 1.

pattern random Ag NWNs, respectively. Figures 3(c,d) show the FOMs for standard and transparent grid-pattern, respectively, made with another material, Al NWNs. Another interesting way of visualizing FOMs is to plot them as $T \times 1/\langle R_s \rangle$ which depicts a decreasing trend (cf. Figure 4). This FOM view highlights an interesting feature related to the material change: Ag NWN systems exhibit slopes that depend more strongly on the AR whereas this feature is weakened in the case of Al NWN systems. This difference is a result of the distinct intrinsic properties (resistivity and extinction coefficient) of each material. Note that the same data points of Figure 3 were re-worked to build Figure 4, however, for the sake of visualization, we used a reduced set of ARs for both random and grid-mesh networks.

We have extensively investigated random Ag NWNs in previous works[16, 29, 30, 35, 36, 59, 81]; we included some of their results here for reference. In all cases, high transparencies are achieved at higher values of AR which translates into "less area coverage". Optical transmissions were improved with the addition of the transparent grid-mesh which serves as a way of controlling the transparency of the devices with the expense of increasing the sheet resistance, especially for NWN systems of sufficiently low densities ($n < 0.5$ nanowires/μm^2). To determine which NWN systems exhibit the best FOMs, we could use a 'distance-to-target'
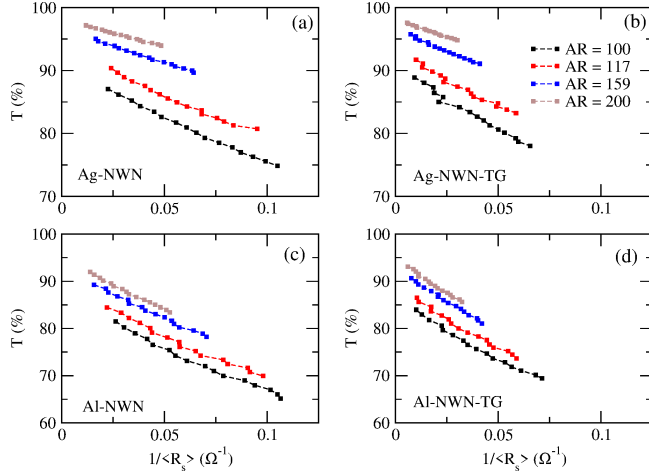
FIG. 4: (color online) Average optical transmittance in percentage (T) versus the inverse of the average sheet resistance ($1/\langle R_s \rangle$) taken for standard random NWNs (left panels) and transparent grid (TG) NWNs (right panels). Top and bottom panels refer to distinct nanowire material, Ag and Al, respectively. Each data point is an average over 10 random NWN samples of fixed density n defined as the number of nanowires per unit of area. All systems are $30 \times 30 \, \mu m$ in size. NWN densities were varied from 0.3 up to 0.7 nanowires/μm^2 in steps of 0.025. TG NWNs were built with a 3×3 transparent grid as depicted in Figure 1. Each line on each panel corresponds to a fixed nanowire aspect ratio (AR) value. To avoid the panels becoming overpopulated with lines, we just present a subset of AR values chosen from Figure 3. The same color legend depicted on panel (b) applies to all other panels.

quantity Δ as

$$\Delta = \sqrt{(T_{max} - T)^2 + (R_{min} - R_s)^2} \tag{3}$$

where, at most ideal conditions, $T_{max} = 1$ (equivalent to 100% optical transmission) and $R_{min} \to 10\,\Omega$ (one of the lowest sheet resistances reported in TCs). Optimum values of (R_s, T) will be the closest to the target coordinate (R_{min}, T_{max}) rendering $\Delta_{min} = \min\{\Delta\}$ as $(R_s \to 10, T \to 1)$. However, Δ is a Euclidean distance that does not account for the distinct units and scales resistance and optical transmission measured. We will then compute standardized Euclidean distance-to-target (Δ_{std}) in which we transform our study variables T and R_s into standardized ones (or Z-score normalization) defined as $z = ((x - \mu))/\sigma_{std}$ where x is the original data set variable, μ is the mean, and σ_{std} is the standard deviation of the data set. We can also work with normalized variables transformed as $z = ((x - x_{min}))/((x_{max} - x_{min}))$ with x_{max} and x_{min} are the maximum and minimum values of the data set, respectively. This analysis can be found in Figure 5. This result demonstrates that it is possible to identify an optimum wire density n, AR, and nanowire material that

11

gives a minimum in Δ_{std}. When contrasting random NWNs with the transparent grid-mesh NWNs, this result also confirms that adding the transparent grid-mesh onto the NWNs improves optical transparency with the expense of increasing sheet resistance. Nonetheless, when weighted equally, this trade-off may provide superior standardized Euclidean distances in comparison to the non-grid random NWNs, particularly for NWNs of larger wire aspect ratios (e.g., $AR = 159$ and $AR = 200$) as demonstrated in Figure 5.
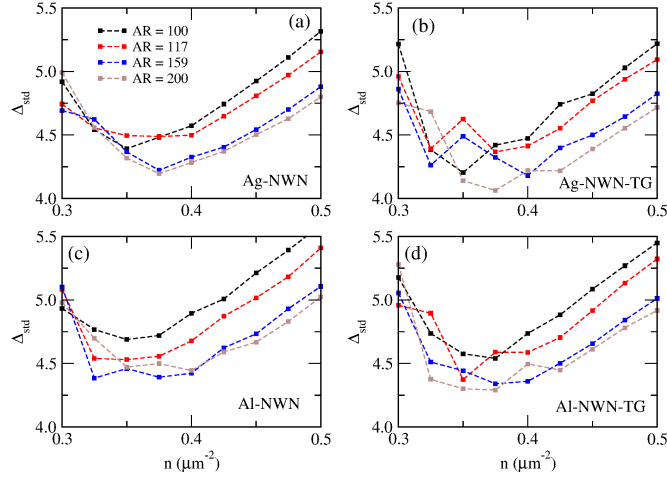
FIG. 5: (color online) Standardized 'distance-to-target' quantity Δ_{std} as a function of wire density n taken for standard random NWNs (a and c panels) and transparent grid (TG) NWNs (b and d panels). Top and bottom panels refer to distinct nanowire material, Ag and Al, respectively. Every data point uses averages over 10 random NWN samples of fixed density n defined as the number of nanowires per unit of area. All systems are $30 \times 30 \, \mu m$ in size. TG NWNs were built with a 3×3 transparent grid as depicted in Figure 1. Each line on each panel corresponds to a fixed nanowire aspect ratio (AR) value. To avoid the panels to become overpopulated with lines and data points, we just present a subset of AR values chosen from Figure 3. The same color legend depicted on panel (a) applies to all other panels.

In addition to the transparent grid-pattern, another means of controlling FOMs in NWN systems is by introducing an angular constraint on the nanowire orientations. Note that the position of the wires continues to be random, what is restricted is the maximum angle to which wires can be oriented with respect to the horizontal axis. Figure 6 presents a compilation of such results for the cases of standard and grid-mesh Ag NWNs with angular constraints. The latter introduces a way of tuning the resistance range of our NWN devices. An additional feature introduced by this strategy is the enhancement of sheet resistance fluctuations in the transparent grid-pattern NWNs. Constraining the nanowire alignment adds a source of fluctuations in the sheet resistance values that we will discuss in detail later
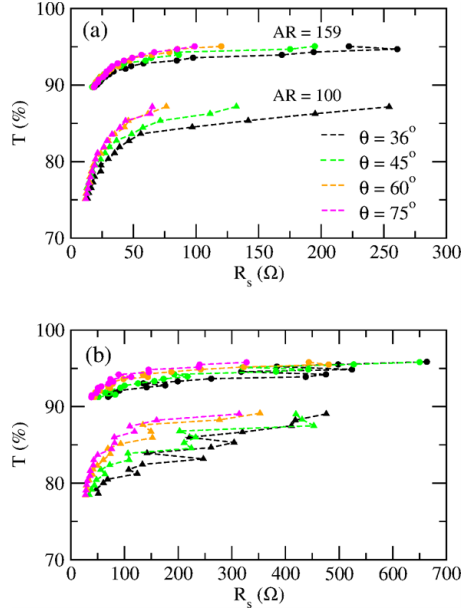
FIG. 6: (color online) Average optical transmittance versus sheet resistance of Ag NWN systems with specific angular orientation of nanowires with respect to the horizontal x-axis. The simulations were carried out for two AR sets: 100 (dashed-upper triangle lines) and 159 (dashed-circle lines). For each AR four maximum angles were set: $\theta_{max} = \pm36^o$, $\pm45^o$, $\pm60^o$, $\pm75^o$ displayed in different color symbols. Each data point is averaged over 10 random spatial configuration ensembles. All systems are $30 \times 30 \, \mu m$ in size. NWN densities were varied from 0.3 up to 0.7 nanowires/μm^2 in steps of 0.025. Panel (a) depicts results for standard random Ag NWNs whereas panel (b) contains the results for transparent grid-pattern Ag NWNs. Transparent grid NWNs were built with a 3×3 transparent grid as depicted in Figure 1.

on when analyzing current flow through the network frame. From all cases studied, $\theta_{max} = \pm75^o$ is characterized to be the dominant alignment angle compared to other alignment trials in terms of obtaining an improved FOM.

FOM results for the last metal addressed in this work (Au NWN systems) are presented in Figure 7. Average optical transmittance versus sheet resistance was obtained for (standard) random and transparent grid-pattern for Au NWNs of distinct ARs. The figure also shows how the sheet resistance of the devices changes with respect to the coverage area fraction (AF). This result demonstrates quantitatively the impact caused by the addition of the transparent grids onto the coverage area of the network. The transparent grids reduce the area coverage by removing sections of material out of the network to which light passes through. By controlling the AF in our devices, we can determine how much transparency gain and sheet resistance loss we wish to engineer in our TC devices. Certainly, all these FOM outcomes are dependent on the use of proper simulation parameters such as material
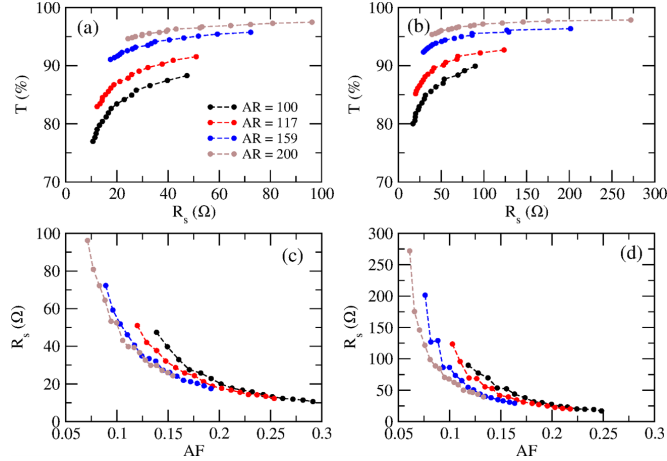
13

FIG. 7: (color online) Top panels depict average optical transmittance in percentage (T) versus average sheet resistance (R_s) results for different nanowire aspect ratios (AR) in (a) random NWNs and (b) transparent grid-pattern NWNs made of Au nanowires. Every data point is averaged over 10 random NWN samples of fixed density. All systems are $30 \times 30\,\mu m$ in size. NWN densities were varied from 0.3 up to 0.7 nanowires/μm^2 in steps of 0.025. Bottom panels display the average sheet resistances versus area fraction (AF) for the same systems studied on the top panels: (c) for standard random Au NWNs and (d) for transparent grid pattern Au NWNs. Transparent grid NWNs were built with a 3×3 transparent grid as depicted in Figure 1.

resistivity, junction resistances, nanowire geometrical aspects, device dimensions and design, optical features, to name but a few. Those can be obtained from ab initio methods or experimental data. We found reliable parameter sources[16, 30, 36, 77, 79, 80] to develop a rich miscellaneous of results relevant to TC research and to demonstrate our robust computational toolkit to study optical transmission versus sheet resistance in a wide variety of NWN systems.

To visually probe the conduction mechanism occurring in the NWNs studied in this manuscript, we performed a spatial characterization of electrical current flow over the NWN systems. This analysis is done by numerically computing the current flow through each nanowire segment on the network and converting this information onto current color maps as depicted in Figure 8. Top panels display current map results for a random and a transparent grid-pattern Ag NWNs. Bottom panels show current maps for a random and transparent grid-pattern Ag NWN with $\theta_{max} = \pm 45^o$ for the nanowires' orientation. One can see that the random NWN exhibits current flow distributed spatially. This trend is altered by the addition of the transparent grids which inhibits the passage of current through certain network sectors. A "current hotspot" can be visualized in the vicinity of the left (source)

14

electrode in Figure 8(b), and this spreads out as we map the current towards the right (drain) electrode. When the angular constraint is introduced, one can say that the current will have a preferred orientation to flow, and this can be seen in Figure 8(c). The transparent grid will partially break this flow as demonstrated in Figure 8(d), and this can result in stronger fluctuations in the sheet resistance when comparing distinct samples with distinct densities. This demonstrates that the transparent grid plus nanowire orientation can be used to control the current flow through the network.
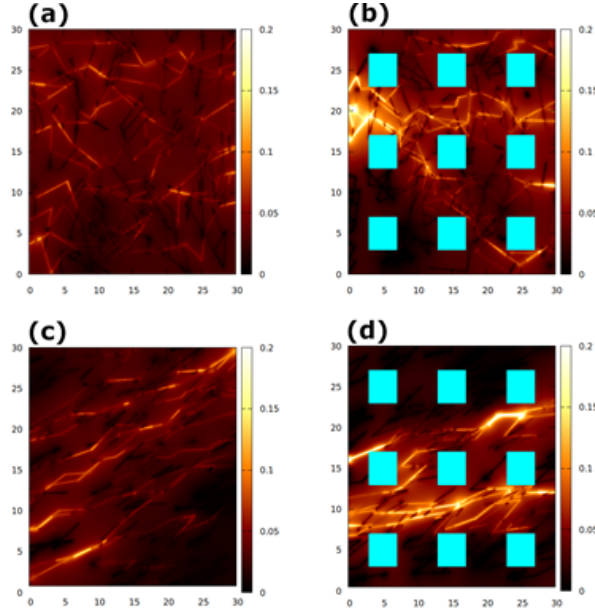

FIG. 8: (color online) Current color maps calculated for distinct Ag NWN layouts. All systems are $30 \times 30 \, \mu m$ in size. The wire density of all networks is fixed at $n = 0.4$ nanowires/μm^2. Color bars display current values in arbitrary units. Top panels (a,b) depict mappings for a random and a transparent grid-pattern NWN, respectively. The transparent grids are represented by cyan squares. Each square is $4 \times 4 \ \mu m$ in size. Bottom panels (c,d) present current mappings for a random and a transparent grid-pattern Ag NWN with the inclusion of constraint on nanowires orientation. In this case, nanowires have a maximum orientation of $\theta_{max} = \pm 45^o$ with respect to the horizontal axis.

Figure 9 shows the averaged EMI SE $\times n$ over AR ranges of $100 - 200$ for different NWN materials (Ag and Au). Figures 9(a,b) present the results for standard and transparent grid-pattern random NWNs, respectively, made with Ag nanowires. Similarly, Figures 9(c,d) depict the EMI SE results for standard and transparent grid-pattern random NWNs, respectively, made with another material, Au nanowires. As expected, SE is considerably larger for standard NWNs compared to transparent grided ones, thus, some shielding mechanism is necessary to ensure the regulation of transmission of the electromagnetic wave across
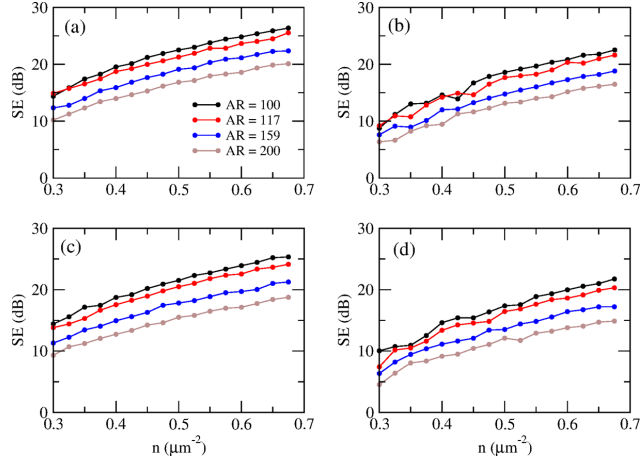
15

FIG. 9: (color online) Average EMI SE (dB) versus density $n\,(\mu m^{-2})$ results for different nanowire aspect ratios ($AR = 100 - 200$). Every data point is averaged over 10 random NWN samples of fixed density. All systems are $30 \times 30\,\mu m$ in size. Top panels (a,b) show results for NWN TC devices made with Ag nanowires whereas bottom panels (c,d) are for Au nanowires. Left panels (a,c) exhibit the EMI SE as a function of density n for standard random NWNs whereas right panels (b,d) are for transparent grid-pattern NWNs. The latter was built with a 3×3 transparent grid as depicted in Figure 1.

the device.

Figure 10 illustrates the Ag hybrid NWNs analysis of networks made of both straight and curved nanowires. We started by determining the average $\langle R_s \rangle$ and $\langle AF \rangle$ of an Ag NWN ensemble of density $n = 0.4\,\mu m^{-2}$ containing purely straight wires and zero curved wires. The density of curved wires is given by n_c and, at this initial state (cf. Figure 10(a)), $n_c = 0$. The next panels present the average $\langle R_s \rangle$ and $\langle AF \rangle$ of an Ag NWN ensemble containing a concentration of curved nanowires in such a way that the total density of the network is kept at $0.4\,\mu m^{-2}$, i.e. $n + n_c = 0.4\,\mu m^{-2}$. Snapshots taken from the NWN ensemble are also presented in the figure for illustration. Our results indicate that the sheet resistance of the network increases with the concentration of curved wires as observed in previous works that investigated percolation effects and resistivity trends of curved NWNs[43, 82]. However, their area fraction is reduced with the addition of curved wires which can benefit optical transparency.

With COMSOL®, we can also determine the electric field scattering planar profiles at given wavelengths as shown in Figure 11 for $\lambda = 560$ nm. The local electric field distributes inhomogeneously around the nanowire circular cross-section, except for Al which is caused by induced electric dipole resonance, and as a result we observe an increase in the intensity

16

of optical extinction and stronger scattering electric field (cf. Fig. S3 in the ESI) [83]. This phenomenon (when the nanowire is much smaller than the wavelength of incident light), strongly relies on the material's composition, geometry, size and dielectric environment of nanowire[84]. The electric field inside the Al nanowire is zero meaning that the displacement of electrons in response to an external electric field causes the polarization of negative and positive charges on the opposite sides of the nanowire; the field produced by these separated charges cancels the external field inside the conductor. This dipole moment production and the dipole strength depend upon the polarizability of the material[85].

Further optical cross-section calculation was carried out on a finite Ag straight and curved nanowire with $D = 50$ nm and $L = 7 \, \mu m$ using COMSOL$^{®}$ Multiphysics software (cf. supplemental information[67]). We have noticed that there is no significant qualitative change in the optical properties of curved and straight Ag nanowires as shown in Figure S4 in the supplemental information[67]. Therefore, for hybrid NWNs in which curved nanowires are embedded in a high dense mesh of numerous wires and connections, their curvature element can be hindered; a curved wire making multiple connections with other wires in the network has its curved segment split into smaller segments of less curvature. Other tests and comparisons between the infinite cylinder and the finite cylinder (of high AR) plus curved cylinder models ran in COMSOL$^{®}$ are presented in the supplemental information[67].

IV. CONCLUSION

In summary, this manuscript presents in-depth electro-optical modeling on metallic NWNs that can be used as transparent conductors. We have developed a comprehensive computational framework to predict the sheet resistance, optical transmittance as well as the electromagnetic interference shielding effectiveness for different NWN designs, namely random NWNs, transparent grid-patterned networks, and NWNs with controlled angular nanowire orientation. We observed that the conduction and optical properties of the films can be tuned by altering the geometrical parameters related to device-design such as grid pattern network alongside relevant network parameters, including aspect ratio and area fraction. Furthermore, the nanowire alignment can be utilized as an additional degree of freedom to manipulate the overall current flow and FOM of the device. The optical response properties were calculated using two methods: Mie light scattering theory and FEM accomplished

by RF module (Wave optics) in COMSOL® Multiphysics software. The methods were set in perfect agreement with each other and could fully capture the electromagnetic scattering properties of metallic nanowires. We have identified that there is an obvious trade-off when employing grid-pattern networks instead of standard random networks by achieving more optical transmittance while hindering conductivity. Calculated EMI SE demonstrates that device layout such as grid-pattern design is a dominant factor and hence it can be re-casted to a certain level of attenuation to meet specific electro-optical criteria. The techniques we carried out in this study will allow us to explore the electro-optical characteristics of nanowire materials for thin metallic films as tunable testbeds before device fabrication in laboratory.
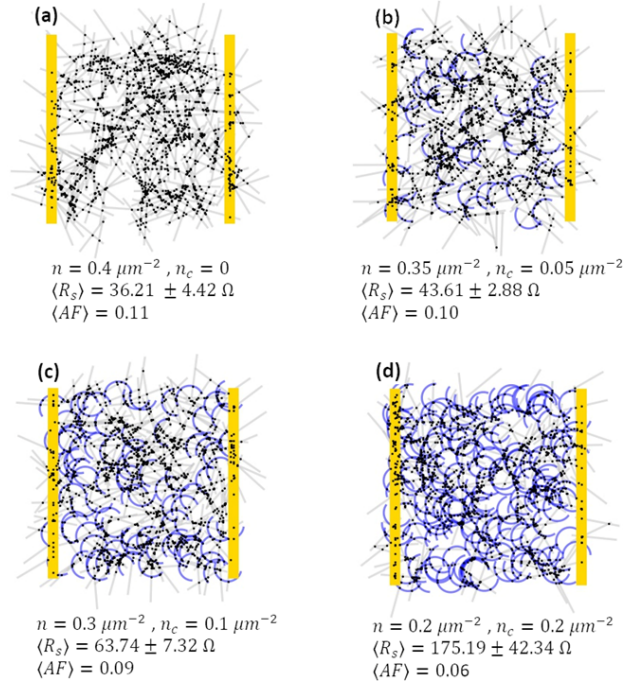

FIG. 10: (color online) Ag NWNs composed of purely straight and hybrid straight/curved nanowires. In all panels, grey and blue lines represent straight and curved nanowires, respectively, and black circles mark their contact points. Golden vertical lines represent metallic electrodes in which a current source (not shown) is attached. The device size is $30 \times 30 \, \mu m$ and straight nanowires' length and curved nanowires' arc length are set to $L = 7 \, \mu m$. The schematics of the networks are just one snapshot out of an ensemble of 10 NWNs from which their respective averaged sheet resistance ($\langle R_s \rangle$), area fraction ($\langle AF \rangle$) are shown in each panel. The standard deviation for R_s is also presented in each panel whereas the standard deviation for AF is of the order of 10^{-4} for all cases studied. n and n_c are the surface densities of straight and curved nanowires, respectively. (a) NWN made of only straight Ag nanowires ($n = 0.4 \, \mu m^{-2}$ and $n_c = 0$). (b-d) Ag hybrid NWNs where n_c increases (n decreases) in such a way to keep the total density of objects fixed at $0.4 \, \mu m^{-2}$.
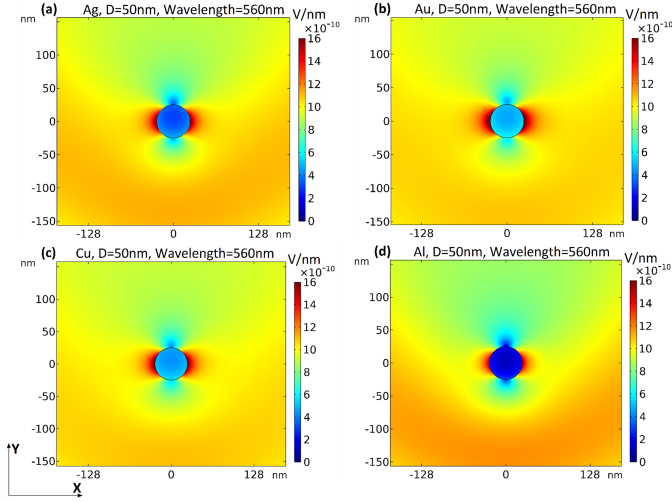
FIG. 11: (color online) The electric field distribution around the circular cross-section in the x-y plane of a nanowire. The nanowires are made of (a) Ag, (b) Au, (c) Cu, and (d) Al with $D = 50$ nm. The cylinder is illuminated by a planewave of $\lambda = 560$ nm whose direction of propagation is along the y-axis with two perpendicular polarizations along x- and z-axis. The color bar shows the electric field intensity (V/nm) simulated based on the averaged of two perpendicular electric field polarizations.

Acknowledgements

[1] D. Tan, C. Jiang, Q. Li, S. Bi and J. Song, *Journal of Materials Science: Materials in Electronics*, 2020, **31**, 15669.

[2] J. Xue, J. Song, Y. Dong, L. Xu, J. Li and H. Zeng, *Science Bulletin*, 2017, **62**, 143.

[3] M. Singh and S. Rana, *Materials Today Communications*, 2020, **24**, 101317.

[4] A. Khan, *Novel Embedded Metal-mesh Transparent Electrodes*, Springer Theses, 2020.

[5] T. Sathiaraj, *Microelectronics Journal*, 2008, **39**, 1444.

[6] P. Kuang, J.-M. Park, W. Leung, R. C. Mahadevapuram, K. S. Nalwa, T.-G. Kim, S. Chaudhary, K.-M. Ho and K. Constant, *Advanced Materials*, 2011, **23**, 2469.

[7] J. van de Groep, P. Spinelli and A. Polman, *Nano Letters*, 2012, **12**, 3138.

[8] T. Sannicolo, M. Lagrange, A. Cabos, C. Celle, J.-P. Simonato and D. Bellet, *Small*, 2016, **12**, 6052.

[9] D. Langley, G. Giusti, C. Mayousse, C. Celle, D. Bellet and J.-P. Simonato, *Nanotechnology*, 2013, **24**, 452001.

[10] W. He and C. Ye, *Journal of Materials Science & Technology*, 2015, **31**, 581.

[11] S. Lee, J. Jang, T. Park, Y. M. Park, J. S. Park, Y.-K. Kim, H.-K. Lee, E.-C. Jeon, D.-K. Lee, B. Ahn and C.-H. Chung, *ACS Appl. Mater. Interfaces*, 2020, **12**, 6169.

[12] H. Wu, D. Kong, Z. Ruan, P.-C. Hsu, S. Wang, Z. Yu, T. J. Carney, L. Hu, S. Fan and Y. Cui, *Nature Nanotechnology*, 2013, **8**, 421.

[13] Y. Yang, S. Chen, W. Li, P. Li, J. Ma, B. Li, X. Zhao, Z. Ju, H. Chang, L. Xiao, H. Xu and Y. Liu, *ACS Nano*, 2020, **14**, 8754.

[14] X. Yu, X. Liang, R. Krishnamoorthy, W. Jiang, L. Zhang, L. Ma, P. Zhu, Y. Hu, R. Sun and C.-P. Wong, *Smart Materials and Structures*, 2020, **29**, 045040.

[15] J. P. Neto, A. Costa, J. V. Pinto, A. Marques–Smith, J. Costa, R. Martins, E. Fortunato, A. R. Kampff and P. Barquinha, *bioRxiv.*, 2020.

[16] H. G. Manning, F. Niosi, C. G. Rocha, A. T. Bellew, C. O'Callaghan, S. Biswas, P. F. Flowers, B. J. Wiley, J. D. Holmes, M. S. Ferreira and J. J. Boland, *Nature Communications*, 2018, **9**, 3219.

[17] Q. Li, A. Diaz-Alvarez, R. Iguchi, J. Hochstetter, A. Loeffler, R. Zhu, Y. Shingaya, Z. Kuncic, K. ichi Uchida and T. Nakayama, *Advanced Functional Materials*, 2020, **30**, 2003679.

[18] S. Bae, S. J. Kim, D. Shin, J.-H. Ahn and B. H. Hong, *Phys. Scr.*, 2012, **2012**, 014024.

[19] R. Zhu, C.-H. Chung, K. C. Cha, W. Yang, Y. B. Zheng, H. Zhou, T.-B. Song, C.-C. Chen, P. S. Weiss, G. Li and Y. Yang, *ACS Nano*, 2011, **5**, 9877.

[20] H. A. Becerril, J. Mao, Z. Liu, R. M. Stoltenberg, Z. Bao and Y. Chen, *ACS Nano*, 2008, **2**, 463.

[21] J. L. Blackburn, T. M. Barnes, M. C. Beard, Y.-H. Kim, R. C. Tenent, T. J. McDonald, B. To, T. J. Coutts and M. J. Heben, *ACS Nano*, 2008, **2**, 1266.

[22] J. C. Bernède, L. Cattin, M. Morsli and Y. Berredjem, *Solar Energy Materials and Solar*

Cells, 2008, **92**, 1508.

[23] S. Pirsalami, S. M. Zebarjad and H. Daneshmanesh, *Journal of Electronic Materials*, 2017, **46**, 4707.

[24] Y. Shi, L. He, Q. Deng, Q. Liu, L. Li, W. Wang, Z. Xin and R. Liu, *Micromachines*, 2019, **10**, 330.

[25] H. Sohn, C. Park, J.-M. Oh, S. W. Kang and M.-J. Kim, *Materials*, 2019, **12**, 2526.

[26] S. Ye, A. R. Rathmell, Z. Chen, I. E. Stewart and B. J. Wiley, *Advanced Materials*, 2014, **26**, 6670.

[27] T. Hauger, A. Zeberoff, B. Worfolk, A. Elias and K. Harris, *Solar Energy Materials and Solar Cells*, 2014, **124**, 247.

[28] B. S. Shim, J. Zhu, E. Jan, K. Critchley and N. A. Kotov, *ACS Nano*, 2010, **4**, 3725.

[29] H. G. Manning, C. G. Rocha, C. O. Callaghan, M. S. Ferreira and J. J. Boland, *Scientific Reports*, 2019, **9**, 11550.

[30] H. G. Manning, P. F. Flowers, M. A. Cruz, C. G. Rocha, C. O. Callaghan, M. S. Ferreira, B. J. Wiley and J. J. Boland, *Applied Physics Letters*, 2020, **116**, 251902.

[31] R. M. Mutiso, M. C. Sherrott, A. R. Rathmell, B. J. Wiley and K. I. Winey, *ACS Nano*, 2013, **7**, 7654.

[32] F. Han, T. Maloth, G. Lubineau, R. Yaldiz and A. Tevtia, *Scientific Reports*, 2018, **8**, 17494.

[33] J. Hwang, H. Sohn and S. H. Lee, *Scientific Reports*, 2018, **8**, 16617.

[34] T. Ackermann, R. Neuhaus and S. Roth, *Scientific Reports*, 2016, **6**, 34289.

[35] J. A. Fairfield, C. G. Rocha, C. O'Callaghan, M. S. Ferreira and J. J. Boland, *Nanoscale*, 2016, **8**, 18516.

[36] A. T. Bellew, H. G. Manning, C. G. Rocha, M. S. Ferreira and J. J. Boland, *ACS Nano*, 2015, **9**, 11422.

[37] I. V. Anoshkin, I. I. Nefedova, I. S. Nefedov, D. V. Lioubtchenko, A. G. Nasibulin and A. V. Räisänen, *Micro & Nano Letters*, 2016, **11**, 343.

[38] S. Sorel, P. E. Lyons, S. De, J. C. Dickerson and J. N. Coleman, *Nanotechnology*, 2012, **23**, 185201.

[39] N. I. Lebovka, Y. Y. Tarasevich, N. V. Vygornitskii, A. V. Eserkepov and R. K. Akhunzhanov, *Physical Review E*, 2018, **98**, 012104.

[40] M.-R. Azani, A. Hassanpour, Y. Y. Tarasevich, I. V. Vodolazskaya and A. V. Eserkepov,

Journal of Applied Physics, 2019, **125**, 234903.

[41] A. Belardini, M. C. Larciprete, M. Centini, E. Fazio, C. Sibilia, D. Chiappe, C. Martella, A. Toma, M. Giordano and F. B. de Mongeot, *Physical Review Letters*, 2011, **107**, 257401.

[42] Z. Yin, S. K. Song, S. Cho, D.-J. You, J. Yoo, S. T. Chang and Y. S. Kim, *Nano Research*, 2017, **10**, 3077.

[43] J. Hicks, J. Li, C. Ying and A. Ural, *Journal of Applied Physics*, 2018, **123**, 204309.

[44] Y. Zhang, J. Guo, D. Xu, Y. Sun and F. Yan, *Nano Research*, 2018, **11**, 3899.

[45] J. A. Fairfield, C. Ritter, A. T. Bellew, E. K. McCarthy, M. S. Ferreira and J. J. Boland, *ACS Nano*, 2014, **8**, 9542.

[46] J. Gu, S. Hu, H. Ji, H. Feng, W. Zhao, J. Wei and M. Li, *Nanotechnology*, 2020, **31**, 185303.

[47] B. Ha and S. Jo, *Scientific Reports*, 2017, **7**, 11614.

[48] S. Sorel, D. Bellet and J. N. Coleman, *ACS Nano*, 2014, **8**, 4805.

[49] M. Lagrange, D. P. Langley, G. Giusti, C. Jiménez, Y. Bréchete and D. Bellet, *Nanoscale*, 2015, **7**, 17410.

[50] F. Shahzad, M. Alhabeb, C. B. Hatter, B. Anasori, S. M. Hong, C. M. Koo and Y. Gogotsi, *Science*, 2016, **353**, 1137.

[51] L.-C. Jia, D.-X. Yan, Y. Yang, D. Zhou, C.-H. Cui, E. Bianco, J. Lou, R. Vajtai, B. Li, P. M. Ajayan and Z.-M. Li, *Advanced Materials Technologies*, 2017, **2**, 1700078.

[52] B. Zhou, M. Su, D. Yang, G. Han, Y. Feng, B. Wang, J. Ma, J. Ma, C. Liu and C. Shen, *ACS Applied Materials & Interfaces*, 2020, **12**, 40859.

[53] X. Zhu, J. Xu, F. Qin, Z. Yan, A. Guoa and C. Kan, *Nanoscale*, 2020, **12**, 14589.

[54] W. Li, H. Zhang, S. Shi, J. Xu, X. Qin, Q. He, K. Yang, W. Dai, G. Liu, Q. Zhou, H. Yu, S. R. P. Silva and M. Fahlman, *Journal of Materials Chemistry C*, 2020, **8**, 4636.

[55] D. G. Kim, J. H. Choi, D.-K. Choi and S. W. Kim, *ACS Applied Materials & Interfaces*, 2018, **10**, 29730.

[56] C. F. Bohren and D. R. Huffman, *Absorption and Scattering of Light by Small Particles*, John Wiley & Sons, 2008.

[57] COMSOL AB, Stockholm, Sweden, *COMSOL Multiphysics$^{®}$*, v. 5.6, `www.comsol.com`.

[58] C. O'Callaghan, C. G. Rocha, H. G. Manning, J. J. Boland and M. S. Ferreira, *Physical Chemistry Chemical Physics*, 2016, **18**, 27564.

[59] C. G. Rocha, H. G. Manning, C. O'Callaghan, C. Ritter, A. T. Bellew, J. J. Boland and M. S.

Ferreira, *Nanoscale*, 2015, **7**, 13011.

[60] I. Vágó, *Graph Theory: application to the calculation of electrical networks*, Elsevier Publishing Company, 1985.

[61] S. Samanta, P. Sarkar, S. Pyne, G. P. Sahoo and A. Misra, *Journal of Molecular Liquids*, 2012, **165**, 21.

[62] S.-C. Lee, *J. Appl. Phys.*, 1990, **68**, 4952.

[63] M. Kerker, *The scattering of light and other electromagnetic radiation*, Academic Press, 1969.

[64] J. Schäfer, *MATSCAT*, MATLAB Central File Exchange, `https://www.mathworks.com/matlabcentral/fileexchange/36831-matscat`.

[65] J.-P. Schäfer, *Implementierung und Anwendung analytischer und numerischer Verfahren zur Lösung der Maxwellgleichungen für die Untersuchung der Lichtausbreitung in biologischem Gewebe*, Univerität Ulm, PhD Thesis, 2011.

[66] J. Schäfer, S.-C. Lee and A. Kienle, *J. Quant. Spectrosc. Radiat. Trans.*, 2012, **113**, 2113.

[67] † ESI.

[68] P. B. Johnson and R. W. Christy, *Physical Review B*, 1972, **6**, 4370.

[69] S. De, P. J. King, P. E. Lyons, U. Khan and J. N. Coleman, *ACS Nano*, 2010, **4**, 7064.

[70] G. Khanarian, J. Joo, X.-Q. Liu, P. Eastman, D. Werner, K. O'Connell and P. Trefonas, *Journal of Applied Physics*, 2013, **114**, 024302.

[71] P. Saini and M. Arora, *New Polymers for Special Applications*, 2012, **3**, 73.

[72] P. Saini, V. Choudhary, B. Singh, R. Mathur and S. Dhawan, *Synthetic Metals*, 2011, **161**, 1522.

[73] P. Saini, V. Choudhary, B. Singh, R. Mathur and S. Dhawan, *Materials Chemistry and Physics*, 2009, **113**, 919.

[74] L.-C. Jia, D.-X. Yan, X. Liu, R. Ma, H.-Y. Wu and Z.-M. Li, *ACS Applied Materials & Interfaces*, 2018, **10**, 11941.

[75] J. Jung, H. Lee, I. Ha, H. Cho, K. K. Kim, J. Kwon, P. Won, S. Hong and S. H. Ko, *ACS Applied Materials & Interfaces*, 2017, **9**, 44609.

[76] H. Wang, C. Ji, C. Zhang, Y. Zhang, Z. Zhang, Z. Lu, J. Tan and L. J. Guo, *ACS Applied Materials & Interfaces*, 2019, **11**, 11782.

[77] E. Sheerin, *A Study on the Fabrication of Seamless Semiconducting and Metallic Nanowire Networks and their Applications for Transparent Electronics*, Trinity College Dublin, PhD

Thesis, 2020.

[78] P. E. Lyons, S. De, J. Elias, M. Schamel, L. Philippe, A. T. Bellew, J. J. Boland and J. N. Coleman, *Journal of Physical Chemistry Letters*, 2011, **2**, 3058.

[79] K. Critchley, B. P. Khanal, M. L. Górzny, L. Vigderman, S. D. Evans, E. R. Zubarev and N. A. Kotov, *Advanced Materials*, 2010, **22**, 2338.

[80] C. Durkan and M. E. Welland, *Physical Review B*, 2000, **61**, 14215.

[81] C. O'Callaghan, C. G. Rocha, F. Niosi, H. G. Manning, J. J. Boland and M. S. Ferreira, *Journal of Applied Physics*, 2018, **124**, 152118.

[82] J. Lee and J. Nam, *Physical Review E*, 2021, **103**, 012126.

[83] W. Li, K. Ren and J. Zhou, *TrAC Trends in Analytical Chemistry*, 2016, **80**, 486.

[84] E. Petryayeva and U. J. Krull, *Analytica Chimica Acta*, 2011, **706**, 8.

[85] W. L. Barnes, *American Journal of Physics*, 2016, **84**, 593.